

Symmetry-protected and Brillouin zone folding driven bound states in the continuum in dielectric nanorod arrays for efficient third harmonic generation

Wen-Jing Wang(王文静), Shi-Jie Liang(梁世杰), Jia-Qi Zou(邹家祺), Yan-Yan Huo(霍燕燕), and Ting-Yin Ning(宁廷银)

Citation: Chin. Phys. B, 2025, 34 (**3**): 034202. DOI: 10.1088/1674-1056/ada2f0
Journal homepage: http://cpb.iphy.ac.cn; http://iopscience.iop.org/cpb

What follows is a list of articles you may be interested in

Interface state-based bound states in continuum and below-continuum-resonance modes with high-*Q* factors in the rotational periodic system

Jialing Yang(杨嘉玲), Aoqian Shi(史奥芊), Yuchen Peng(彭宇宸), Peng Peng(彭鹏), and Jianjun Liu(刘建军)
Chin. Phys. B, 2024, 33 (**8**): 084206. DOI: 10.1088/1674-1056/ad4630

Mode coupling with Fabry-Perot modes in photonic crystal slabs

Ken Qin(秦恳), Peng Hu(胡鹏), Jie Liu(刘杰), Hong Xiang(向红), and De-Zhuan Han(韩德专)
Chin. Phys. B, 2024, 33 (**8**): 084205. DOI: 10.1088/1674-1056/ad4ff8

Enhancing the Goos-Hänchen shift based on quasi-bound states in the continuum through material asymmetric dielectric compound gratings

Xiaowei Jiang(江孝伟), Bin Fang(方彬), and Chunlian Zhan(占春连)
Chin. Phys. B, 2024, 33 (**3**): 034206. DOI: 10.1088/1674-1056/acf661

Evolution of polarization singularities accompanied by avoided crossing in plasmonic system

Yi-Xiao Peng(彭一啸), Qian-Ju Song(宋前举), Peng Hu(胡鹏), Da-Jian Cui(崔大健), Hong Xiang(向红), and De-Zhuan Han(韩德专)
Chin. Phys. B, 2023, 32 (**1**): 014201. DOI: 10.1088/1674-1056/ac728d

Bound states in the continuum in metal—dielectric photonic crystal with a birefringent defect

Hongzhen Tang(唐宏珍), Peng Hu(胡鹏), Da-Jian Cui(崔大健), Hong Xiang(向红), and Dezhuan Han(韩德专)
Chin. Phys. B, 2022, 31 (**10**): 104209. DOI: 10.1088/1674-1056/ac6db6

Symmetry-protected and Brillouin zone folding driven bound states in the continuum in dielectric nanorod arrays for efficient third harmonic generation

Wen-Jing Wang(王文静)[1,2], Shi-Jie Liang(梁世杰)[1,2], Jia-Qi Zou(邹家祺)[1,2], Yan-Yan Huo(霍燕燕)[1,2], and Ting-Yin Ning(宁廷银)[1,2,†]

[1] *Shandong Provincial Engineering and Technical Center of Light Manipulations & Shandong Provincial Key Laboratory of Optics and Photonic Device, School of Physics and Electronics, Shandong Normal University, Jinan* 250358, *China*

[2] *Collaborative Innovation Center of Light Manipulation and Applications, Shandong Normal University, Jinan* 250358, *China*

(Received 28 August 2024; revised manuscript received 16 December 2024; accepted manuscript online 24 December 2024)

Two types of bound states in continuum (BICs), symmetry-protected and Brillouin zone folding driven, are identified in hollow Si nanorod arrays. By modulating the direction and distance of the air holes from the center of the nanorods, it is possible to achieve either a single quasi-BIC or three quasi-BICs. The transmission spectra exhibit ultra-narrow lines, and the quasi-BICs demonstrate ultra-high Q factors. Additionally, efficient third-harmonic generation occurs at low pump intensities. The results indicate that the proposed nanostructures of two types of BICs with a flexible modulation hold great potential applications for nonlinear photonic devices.

Keywords: bound states in the continuum, Brillouin zone folding, third harmonic generation

PACS: 42.65.Ky, 42.70.Qs, 71.20.–b

DOI: 10.1088/1674-1056/ada2f0 **CSTR:** 32038.14.CPB.ada2f0

1. Introduction

Third harmonic generation (THG), three photons of frequency ω converting into one photon of frequency 3ω, has important applications in frequency conversion,[1] optical communication,[2] spectral analysis,[3,4] and optical imaging.[5–7] In recent years, significant attention has been devoted to the exploring of subwavelength resonators which possess ultra-high quality factors (Q-factor) to enhance the THG process.[8–12] The advent of bound states in the continuum (BICs) gives a groundbreaking way to attain unparalleled Q-factor levels and local field enhancement.[13–22] Quasi-BIC is an optical mode partially bound to the structure yet coupled to the continuum, typically characterized by finite Q-factors and non-zero linewidths for practical applications.[13]

Recently, silicon (Si) photonic devices have exhibited attractive properties in ultra-large-scale monolithic optoelectronic integration, as well as high-speed modulation and switching.[23–25] Si, renowned for its compatibility with the existing complementary metal–oxide–semiconductor (CMOS) processes,[26–30] possesses unique characteristics, including high refractive index and strong third-order optical nonlinearity.[31–34] Consequently, Si emerges as an ideal candidate for achieving quasi-BICs and leveraging its attributes for nonlinear optics applications.[33,35,36]

In this paper, we investigate the BICs and the corresponding efficient THG optical responses of periodically arranged arrays of hollow Si nanorods. Two types of BICs, i.e., symmetry-protected BIC and Brillouin zone folding (BZF) driven BIC, are both obtained within these nanostructures. One quasi-BIC mode resulting from the symmetry breaking and two BZF driven BICs are observed when the air holes are shifted away from the center of nanorods. The efficient THG is achieved at low pump intensities, facilitated by the ultra-high Q-factor and significant local field enhancement of the quasi-BICs. The results indicate that the proposed nanostructures are promising in applications for integrated nonlinear photonic devices.

2. Designed structures and numerical simulation

The structure of the hollow Si nanorods arrays is schematically depicted in Fig. 1. Figure 1(a) shows the primary hollow Si nanorod array with air holes at the center of Si. The radius of the Si nanorod is $R = 350$ nm, the gap width is $d = 280$ nm, and the radius of the air hole is $r = 100$ nm. The period $P = 2R + d$ is 980 nm. For the two adjacent nanorods, the shifts of the left and right air holes are denoted as $\delta_{\rm l}$ and $\delta_{\rm r}$, respectively. Figure 1(b) presents all the air holes shifted in the same direction with $\delta_{\rm l} = \delta_{\rm r}$ or $\delta_{\rm l} \neq \delta_{\rm r}$. Figure 1(c) depicts the left and right air holes in the adjacent nanorods shifted in the opposite directions. The proposed nanostructures are probably fabricated experimentally. First, a layer of photoresist is coated on the Si substrate, and an electron beam lithography technique along with the lift-off process is used to fabricate the desired hollow nanostructure array on it. Second, an Au

[†]Corresponding author. E-mail: ningtingyin@sdnu.edu.cn

© 2025 Chinese Physical Society and IOP Publishing Ltd. All rights, including for text and data mining, AI training, and similar technologies, are reserved.

layer is thermally evaporated onto the Si substrate with the desired hollow photoresist array. Finally, the sample is placed in a mixed solution of H_2O, HF and H_2O_2 at room temperature for etching. Due to the significantly higher etching rate of Si substrate covered by Au compared to those that are not covered,[37] hollow Si nanowires are achieved after removing the photoresist and Au. Such structures of extreme aspect ratios can be realized experimentally.[38–42]

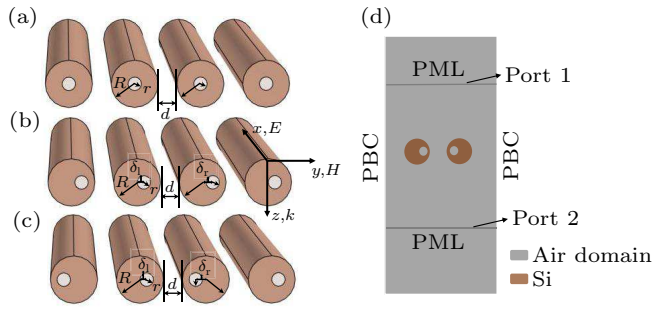


Fig. 1. Schematic of (a) hollow Si nanorod array with air holes at the center of Si. Air holes shift away from the center of Si nanorods (b) in the same direction and (c) in the opposite directions. (d) The settings of the numerical model in Comsol Multiphysics. PML and PBC indicate the perfect matching layer and periodic boundary condition, respectively.

The electric field $\boldsymbol{E}$ of light is along with the x-axis direction, i.e., transverse electric (TE) polarization of light is considered. Unless otherwise specified, the amplitude of the electric field of the light is set as $E = 10^5$ V/m, and the corresponding intensity is around 2.65 kW/cm^2. The wave equation of the fundamental and THG fields in the frequency domain (time-harmonic factor $\exp(-\mathrm{i}\omega t)$) under the undepleted pump approximation can be described as[1,13]

$$\nabla\times\nabla\times\boldsymbol{E}(\omega)-k_1^2\boldsymbol{E}(\omega)=\mu_0\omega^2\boldsymbol{P}^{(1)}(\omega), \quad (1)$$

$$\nabla\times\nabla\times\boldsymbol{E}(3\omega)-\varepsilon_3 k_3^2\boldsymbol{E}(3\omega)=\mu_0(3\omega)^2\boldsymbol{P}^{(3)}(3\omega), \quad (2)$$

where $\boldsymbol{E}(\omega)$ and $\boldsymbol{E}(3\omega)$ are fundamental and THG electric fields, $k_1 = \omega/c$ and $k_3 = 3\omega/c$ are the wave vectors of the fundamental and TH beams, respectively. c is the speed of light in a vacuum. μ_0 is the vacuum permeability. ε_3 is the relative permittivity of material at TH frequency. $\boldsymbol{P}^{(1)}(\omega) = \varepsilon_0\chi^{(1)}(\omega)\boldsymbol{E}(\omega)$ and $\boldsymbol{P}^{(3)}(3\omega) = \varepsilon_0\chi^{(3)}(3\omega)\vdots\boldsymbol{E}(\omega)\boldsymbol{E}(\omega)\boldsymbol{E}(\omega)$ are linear polarization at the fundamental frequency and nonlinear polarization at the THG frequency. ε_0 is the vacuum permittivity. For tensor components of the third-order susceptibility $\chi^{(3)}$ of Si, only $\chi^{(3)}_{zzzz}$ is considered of the value $\chi^{(3)}_{zzzz} = 2.45\times10^{-19}$ m^2/V^2, and then $\boldsymbol{P}^{(3)}_z(3\omega) = \varepsilon_0\chi^{(3)}_{zzzz}\boldsymbol{E}_z(\omega)\boldsymbol{E}_z(\omega)\boldsymbol{E}_z(\omega)$.

Numerical simulations are conducted using the finite element method via the commercial software Comsol Multiphysics. The band structures are first conducted using the eigenfrequency analysis. Then, the linear transmittance and THG are obtained by solving the coupled Eqs. (1) and (2). Detailed settings can be referred to Ref. [13], as shown in Fig. 1(d). Briefly, the top and bottom boundaries of the air domain containing the silicon nanorods are assigned to be port 1 and port 2, respectively. The perfectly matched layers (PMLs) are attached to the outside of two ports. Periodic boundary conditions (PBCs) are applied to the left and right sides of the simulation domain. The Floquet periodicity vector k_F is set to 0 at the normal incidence. The refractive index of air is 1. The refractive index of Si at the FW and THG wavelengths are 3.42 and $3.8+0.014$i, respectively.[43,44] The linear permittivities are 11.6964 and $14.4398+0.1064$i, respectively. The phase mismatch of colinear FW and THG waves is $\Delta k = k_3 - 3k_1$. The coherent length $L_{\mathrm{coh}} = \pi/\Delta k$ ranges from 0.83 μm to 0.95 μm at the FW wavelength from 1900 nm to 2160 nm, which is larger than the thickness of nanostructures. In our simulation, the transmitted THG power is obtained by integrating the Poynting vector of THG waves along port 2. The phase mismatch of FW and THG is involved. The whole model includes two steps: first, the linear properties of the nanostructure are calculated, including the transmittance of the fundamental wave, the electric field $\boldsymbol{E}(\omega)$ at the resonance modes, and the Q-factor. The Q-factor is defined as $Q = \lambda/\Delta\lambda$, where λ represents the resonance wavelength, and $\Delta\lambda$ is the difference in wavelength between the peak and valley;[45] second, the nonlinear optical properties of the nanostructures are calculated by using the fundamental electric field calculated in the first step, including the THG conversion efficiency η and the electric field $\boldsymbol{E}(3\omega)$ distribution at the resonance modes. The conversion efficiency is defined as $\eta = P_{(3\omega)}/P_{\mathrm{in}}$, where P_{in} and $P_{(3\omega)}$ denote the power of fundamental light and transmitted THG light from port 2.

3. Results and discussion

The band structure of nanostructures with the air holes centered in the Si nanorods (i.e., $\delta_l = \delta_r = 0$ nm) by eigenfrequency analysis is shown in Fig. 2(a). Four bands are presented with dots when a single hollow Si nanorod is chosen as a unit cell with the period P. The corresponding Q-factors are given as dotted line-circles in Fig. 2(b). It is worth noting that there are three BIC modes of infinite Q-factor at bands 1 ($k_x = 0$), 2 ($k_x = \pm\pi/P$) and 4 ($k_x = \pm\pi/P$). The BIC at band 1 when $k_x = 0$ (Γ point) corresponds to the symmetry-protected BIC. The BICs at bands 2 and 4 when $k_x = \pm\pi/P$ is below the light line, and thus have no coupling with the environment. When two adjacent hollow Si nanorods are chosen as a unit cell with period $2P$, four bands are depicted with solid lines. As the period is doubled, the first BZ is folded, as shown in the lower inset of Fig. 2(a). The bands will also be folded. Bands 1 and 3 both in the single unite cell BZ and period-doubled BZ are exactly overlapped. Bands 2 and 4 in the single unite cell BZ in the range of $-\pi/P$ to $-\pi/(2P)$ and $\pi/(2P)$ to π/P fold into the period doubled BZ ($-\pi/(2P)$ to $\pi/(2P)$). The BICs at $k_x = \pm\pi/P$ fold to the $k_x = 0$, and the

BICs are both above the light line and below the folded light line, as shown in the upper inset of Fig. 2(a). The BICs thus become quasi-BICs. The corresponding Q-factors are given as solid lines in Fig. 2(b). The eigenfrequencies of the four modes at $k_x = 0$ in the box A (Fig. 2(a)) are 154.52 THz, 151.1 THz, 145.93 THz, and 138.68 THz, respectively. The corresponding electric field distributions of the four modes are presented on the right-hand side of Fig. 2(a).

In the following sections, we will investigate the BICs transformed into quasi-BICs with the shift of air holes away the center of Si nanorods and the corresponding THG responses.

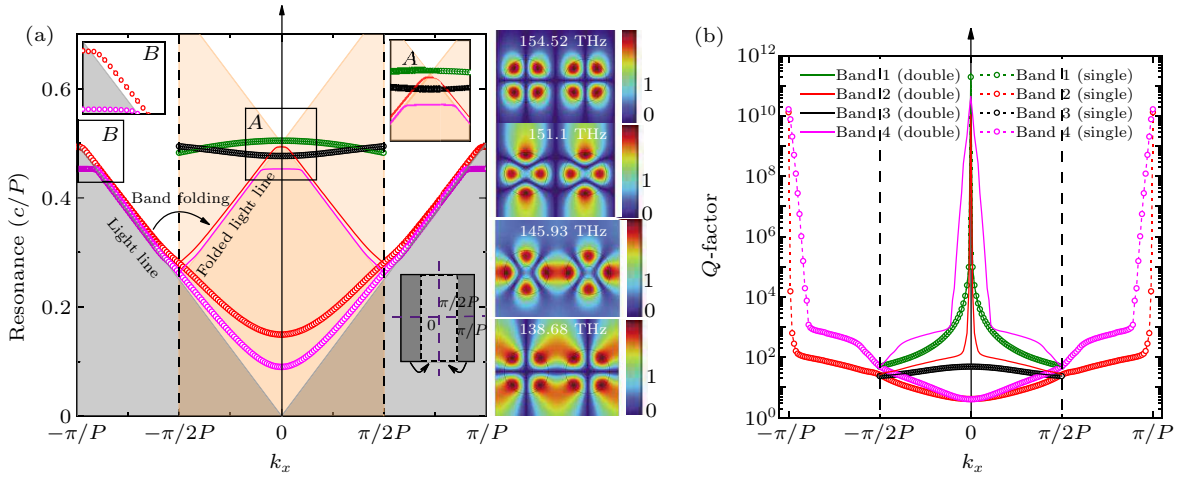


Fig. 2. (a) The band structure of nanorod arrays calculated under a single- (circles) and double-cycle (solid lines). The upper insets show zooms of boxes A and B, and the lower inset shows the Brillouin zone. The normalized field distribution at the four resonances is shown on the right-hand side. (b) The Q-factors of the four bands in (a) under a single- (dotted line-circles) and double-cycle (solid lines), respectively.

3.1. Air holes shifted in the same direction of the same distance

Under such geometry, only symmetry-protected BIC mode becomes the quasi-BIC mode since the period is not changed. The linear transmittance of nanostructures of different $\delta_l = \delta_r$ is shown in Fig. 3. The transmittance of the primary nanostructure of $\delta_l = \delta_r = 0$ nm is also given as a reference. The broad Fano resonance at 145.93 THz corresponds to band 3 in Fig. 2(a) of low Q-factor at $k_x = 0$ (Fig. 2(b)). It is always a radiation mode. The quasi-BIC modes at around 154.52 THz appear when the $\delta_l = \delta_r \neq 0$ nm due to the symmetry breaking. The mode is just from the BIC at band 1 when $k_x = 0$. The detailed resonance of the two modes under different $\delta_l = \delta_r$, along with the corresponding field distribution in the nanostructure $\delta_l = \delta_r = 40$ nm, are shown in Figs. 3(b) and 3(c), respectively. The field distributions agree with those obtained by eigenfrequency analysis (Fig. 2). The line shape becomes broader as the increase of asymmetry as predicted. The dependence of Q-factors of the two modes on the $\delta_l = \delta_r$ is given in Fig. 3(d). The Q-factor at quasi-BIC mode reaches up to 1.87×10^5 at $\delta_l = \delta_r = 10$ nm and 2.21×10^4 at $\delta_l = \delta_r = 30$ nm. Such large Q-factor enables the efficient nonlinear optical response in the nanostructures.

The THG response in such the nanorod arrays is then investigated, as shown in Fig. 4(a). It can be observed that THG conversion efficiency at the quasi-BIC I decreases with the increase of $\delta_l = \delta_r$. The maximum conversion efficiency occurs at $\delta_r = 10$ nm of 1×10^{-6}. The dependence of third harmonic conversion efficiency on the fundamental intensity in the nanostructure of $\delta_l = \delta_r = 40$ nm at the two resonant modes is given in Fig. 4(b). The slope is 2, as expected. The corresponding distributions of THG electric field are presented in Figs. 4(c) and 4(d), respectively.

3.2. Air holes in the two adjacent nanorods are shifted in the same direction of different distances

Under such geometry, besides the symmetry breaking of a single nanorod, the period is doubled, and thus the symmetry-protected BIC and two BZF driven BICs can transform into the quasi-BICs. Without loss of generality, we fix the $\delta_l = 50$ nm and change the δ_r ranging from 0 nm to 90 nm. The linear transmittance of different nanostructures is shown in Fig. 5(a). The three quasi-BICs are obviously observed except when $\delta_l = \delta_r = 50$ nm, which returns to the above geometry, and only the BIC I. The two BZF driven BICs at around 151.1 THz and 138.68 THz are denoted as BIC II and BIC III, respectively. Figures 5(b)–5(e) show the transmittance around the four modes in the different nanostructures. The distributions of the local fields in the $\delta_r = 40$ nm nanostructure are given at the corresponding resonant modes, and also agree well with those obtained by eigenfrequency analysis (Fig. 2). The dependence of Q-factors of the four modes on the δ_r is shown in Fig. 5(f). The Q-factor of BIC I decreases with the increase of δ_r. The two quasi-BZF driven BICs have the infinite Q-factor as $\delta_r = 50$ nm, since the nanostructures return to be the above configure of the single period when $\delta_r = 50$ nm. The Q-factor decrease as δ_r far away 50 nm. The Q-factor of quasi-BIC III mode is the highest among different geometrical parameters, and reaches around 3×10^6 for $\delta_r = 60$ nm.

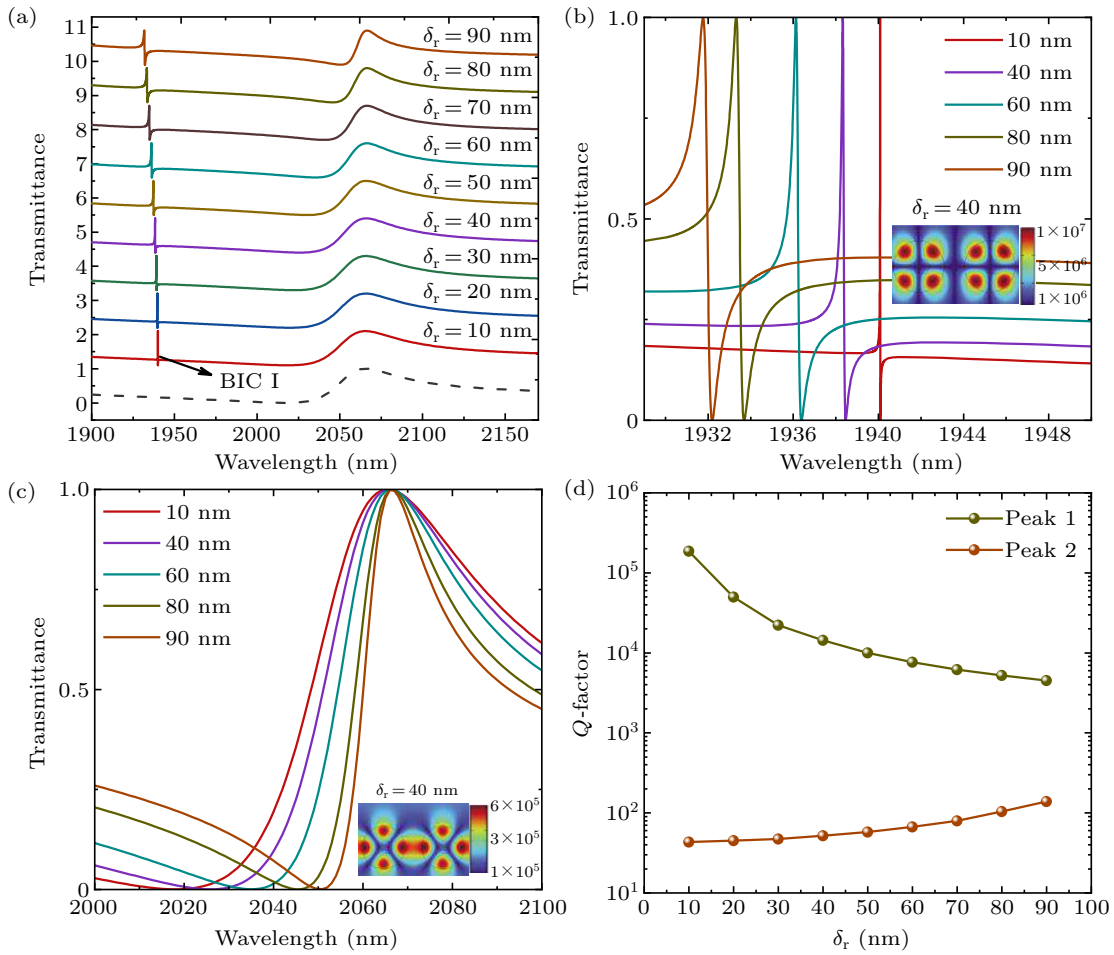


Fig. 3. (a) The transmission spectra of Si nanorods array as the air holes shift away the center in the same direction of the same amounts, i.e., $\delta_l = \delta_r$. The dashed line represents the transmission spectrum as $\delta_l = \delta_r = 0$ nm. (b) and (c) The transmission spectra around the two resonance modes. The inset shows the field distribution of the unit V/m in the nanostructure of $\delta_l = \delta_r = 40$ nm at the corresponding resonant modes. (d) Dependence of Q-factors on offset δ_r. Peak 1 and peak 2 represent the BIC I and Fano resonances, respectively.

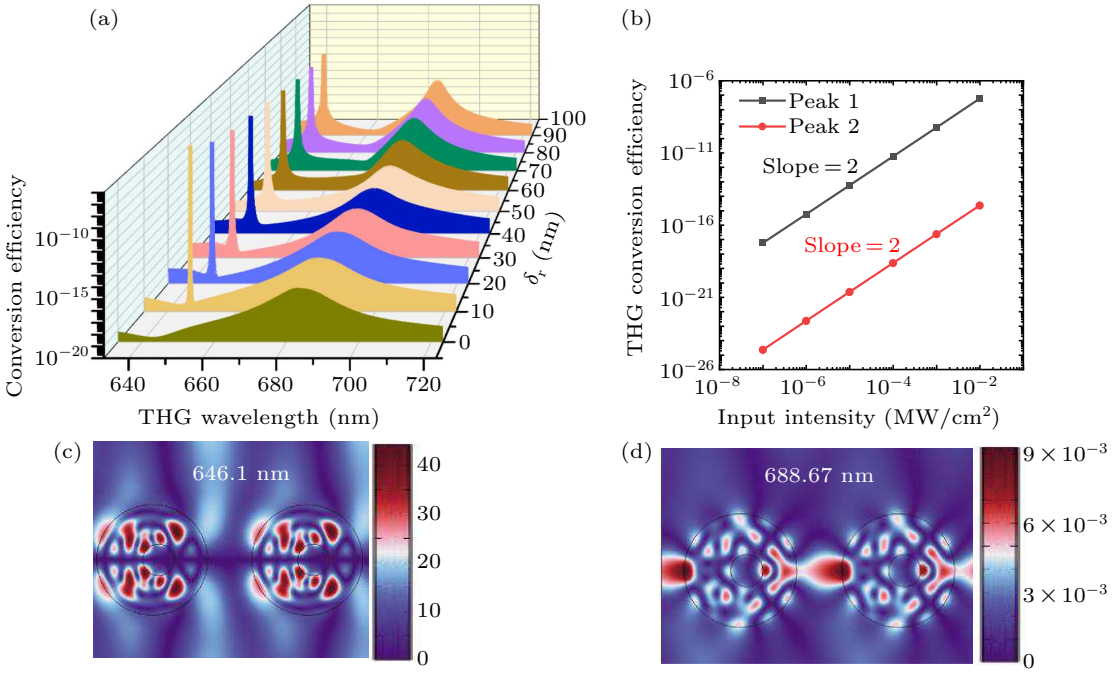


Fig. 4. (a) The THG conversion efficiency in the nanostructures of different $\delta_l = \delta_r$. (b) The dependence of THG conversion efficiency on the fundamental intensity, (c) and (d) the distributions of THG electric field of the unit V/m, in the nanostructure of $\delta_l = \delta_r = 40$ nm at the two resonant modes, respectively.

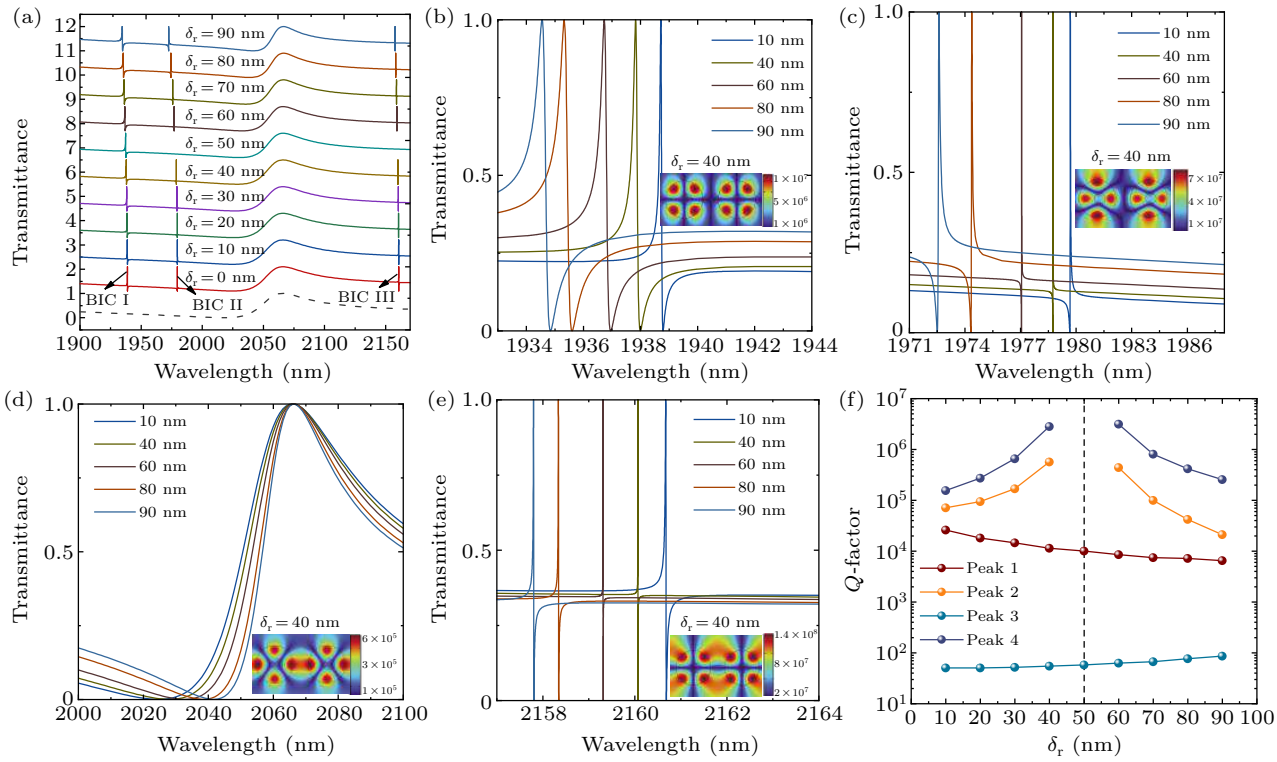


Fig. 5. (a) The transmission spectra of Si nanorod arrays as the air holes shift away the center in the same direction of different amounts, i.e., $\delta_l = 50$ nm, while δ_r varies from 0 to 90 nm. The dashed line represents the transmission spectrum as $\delta_l = \delta_r = 0$ nm as the reference. (b)–(e) The transmittance around the four modes in the different nanostructures. These insets show the distributions of local field in the nanostructure of $\delta_r = 40$ nm at the corresponding resonant mode. The accompanying figures show the distribution of the fundamental electric fields of the unit V/m at the resonant wavelength of $\delta_r = 40$ nm. (f) The dependence of Q-factors of the four modes on the δ_r.

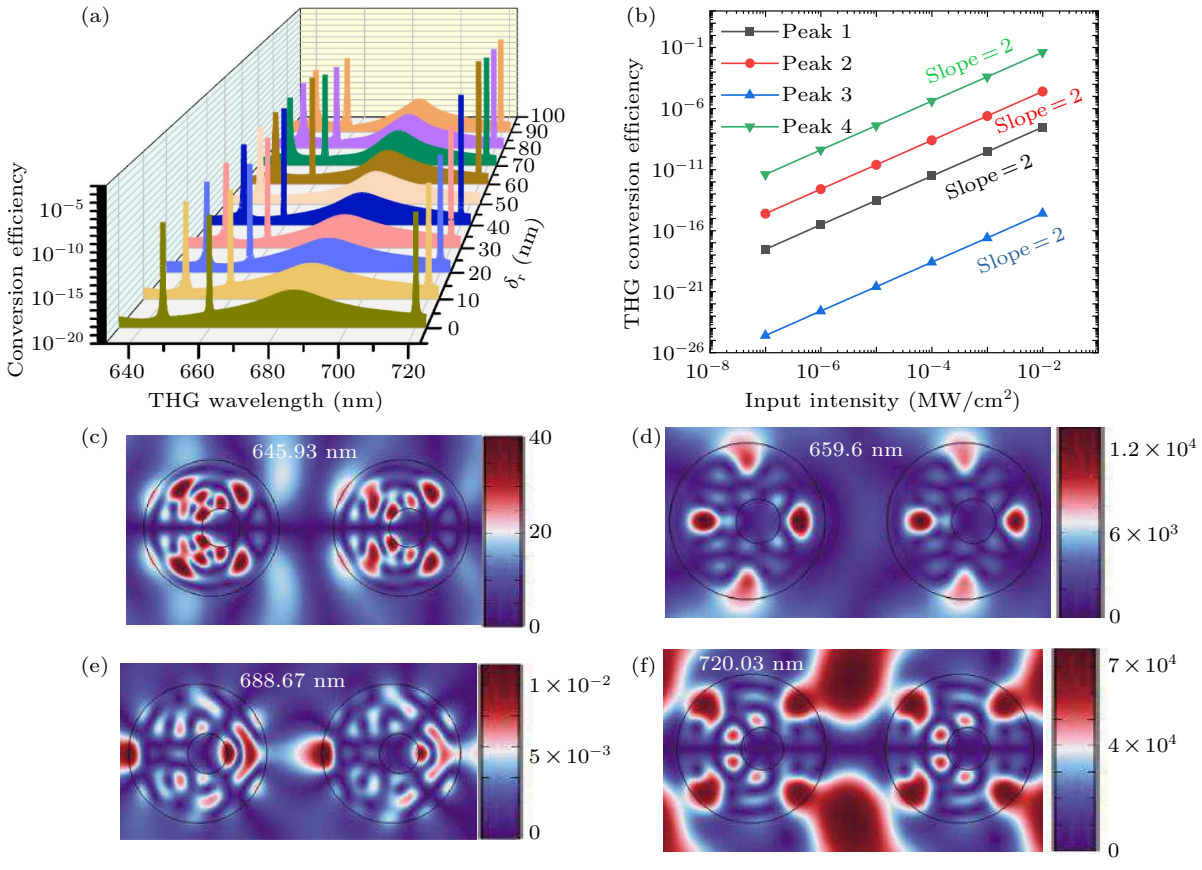


Fig. 6. (a) The THG conversion efficiency in the nanostructures of different δ_r. (b) The dependence of THG conversion efficiency in the nanostructure of $\delta_r = 40$ nm at the resonant mode on the fundamental intensity. The slopes are all 2. (c)–(f) The distributions of THG electric field of the unit V/m at the corresponding resonant mode, respectively.

The THG response in such configurations is then numerically calculated, as shown in Fig. 6(a). The highest THG conversion efficiency occurs at the quasi-BIC III mode when the δ_r is close to 50 nm among the four resonant modes. It reaches a value of 9.6×10^{-2} in the nanostructure of $\delta_r = 60$ nm. The dependence of THG conversion efficiency on the fundamental intensity in the nanostructure of $\delta_r = 40$ nm at the four resonant modes is given in Fig. 6(b). The corresponding distributions of THG electric field are shown in Figs. 6(c)–6(f), respectively.

3.3. Air holes in the two adjacent nanorods are shifted in the opposite directions

Finally, we study the optical phenomena in the nanorods array when the air holes are shifted in the opposite directions. Under such configuration, as the structure in Subsection 3.2, the symmetry of a single nanorod is broken and the period is also doubled, and thus three quasi-BICs can be formed from the symmetry-protected BIC and two BZF driven BICs.

The band structure and Q-factor diagrams are first analyzed by eigenfrequency analysis, as shown in Fig. 7. The band structures in the nanostructure when the two adjacent air holes have the same ($\delta_l = \delta_r = 50$ nm) and different ($\delta_l = 50$ nm, $\delta_r = 20$ nm) shifts are shown in Figs. 7(a) and 7(f), and the corresponding Q-factors of the four bands in each geometry of nanostructure are given in Figs. 7(b) and 7(g), respectively. The first two bands (eigenfrequencies around 154.77 THz and 151.53 THz) have infinite Q-factor at $k_x = 0$ in the nanostructure of the same amount of shift besides $\delta_l = \delta_r = 50$ nm, and only band 4 becomes quasi-BIC of the finite Q-factor. This can be explained from the electric field distribution, as shown in Figs. 7(c)–7(e). When the two adjacent

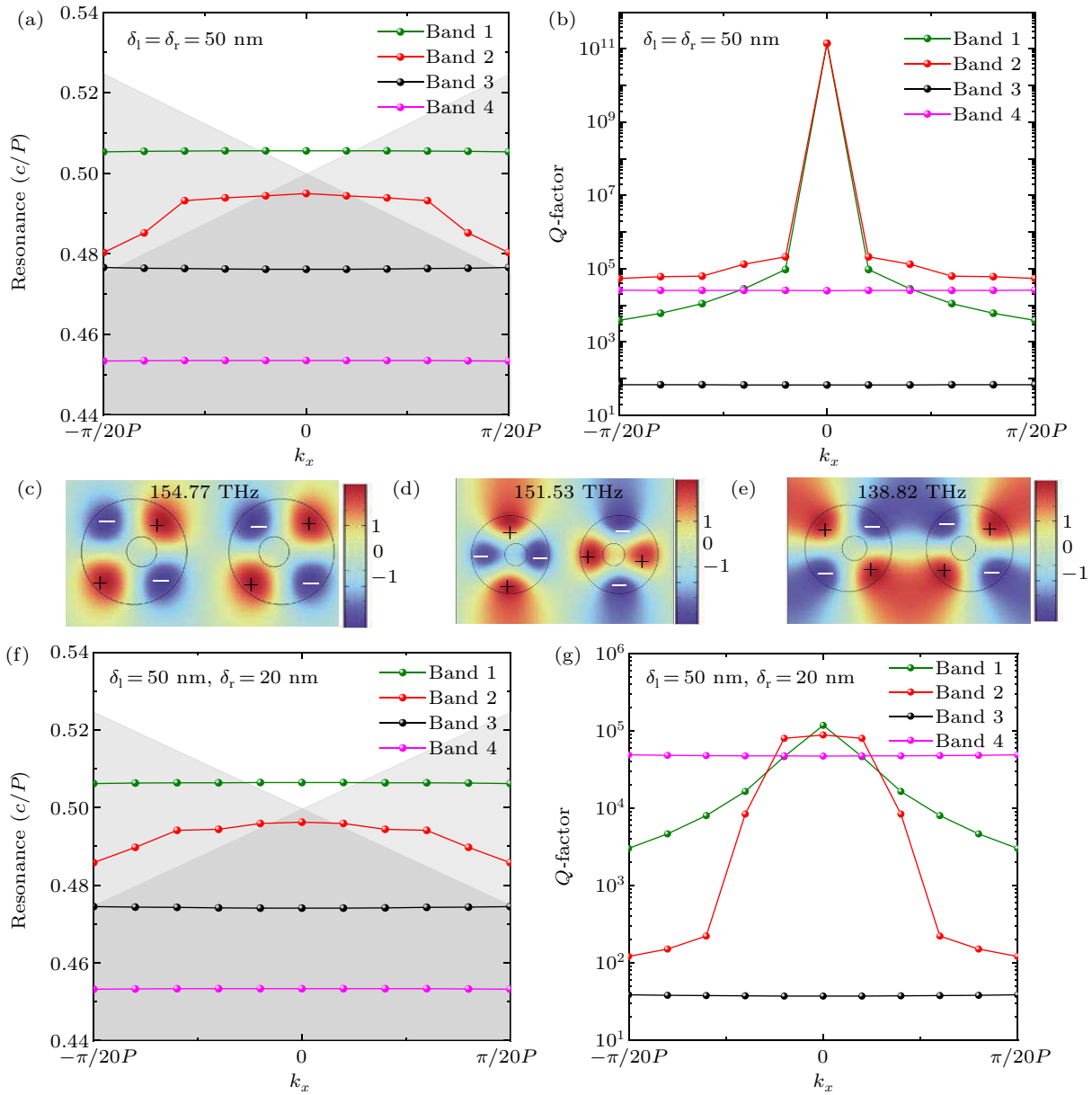


Fig. 7. The band structure of nanorod arrays when (a) $\delta_l = \delta_r = 50$ nm and (f) $\delta_l = 50$ nm,$\delta_r = 20$ nm. The Q-factors of the four bands in each geometrical configuration are given in (b) and (g). (c)–(e) The normalized electric filed E_z distribution at resonance modes in the structure of $\delta_l = \delta_r = 50$ nm.

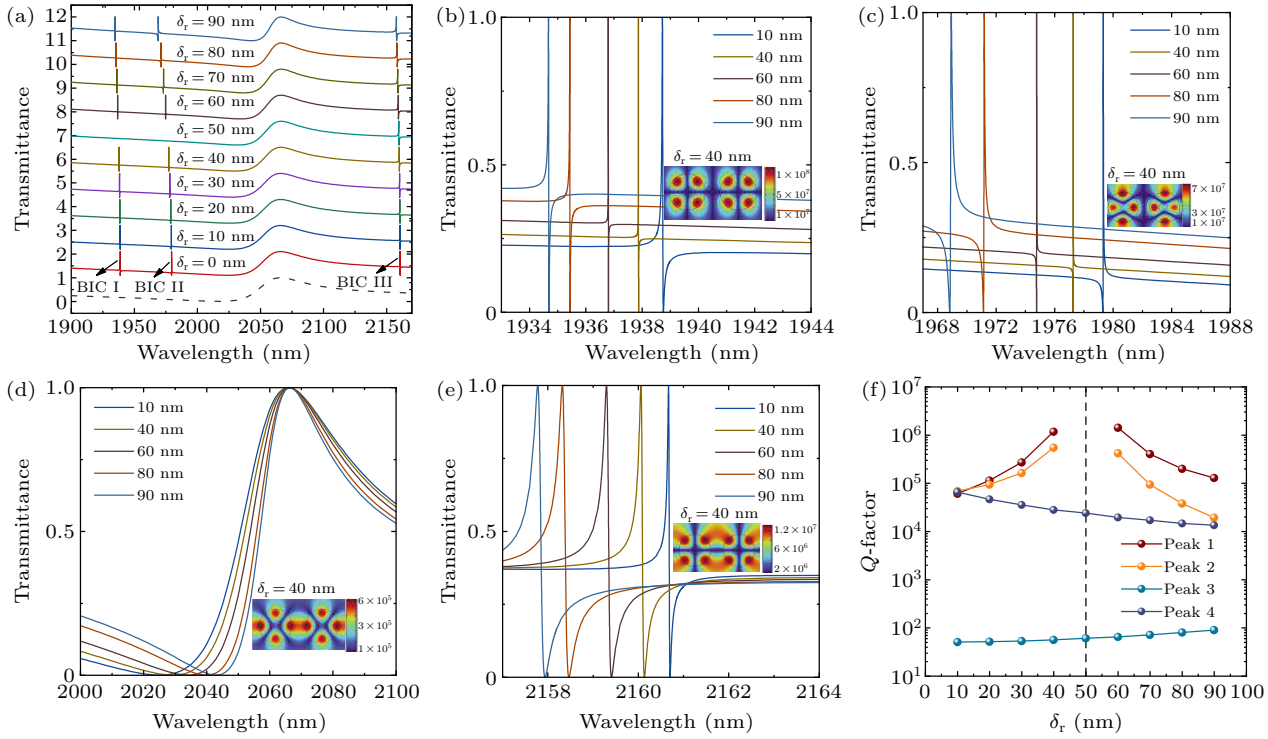


Fig. 8. (a) Comparison of transmission spectra of air pillars shifted to the left by different amounts (fixed $\delta_l = 50$ nm, δ_r taken in increments of 10 nm from 0 nm to 90 nm), where the dashed line represents the transmission spectrum of the air pillars at the center of the silicon column. Meanwhile, (b)–(e) represent the variation of the resonance wavelength with offset δ_r for BIC I, BIC II, Fano resonance, and BIC III, respectively. The accompanying figures display the distribution of the fundamental electric fields of the unit V/m at the resonant wavelength at $\delta_r = 40$ nm. (f) The relationship between Q-factors and offset.

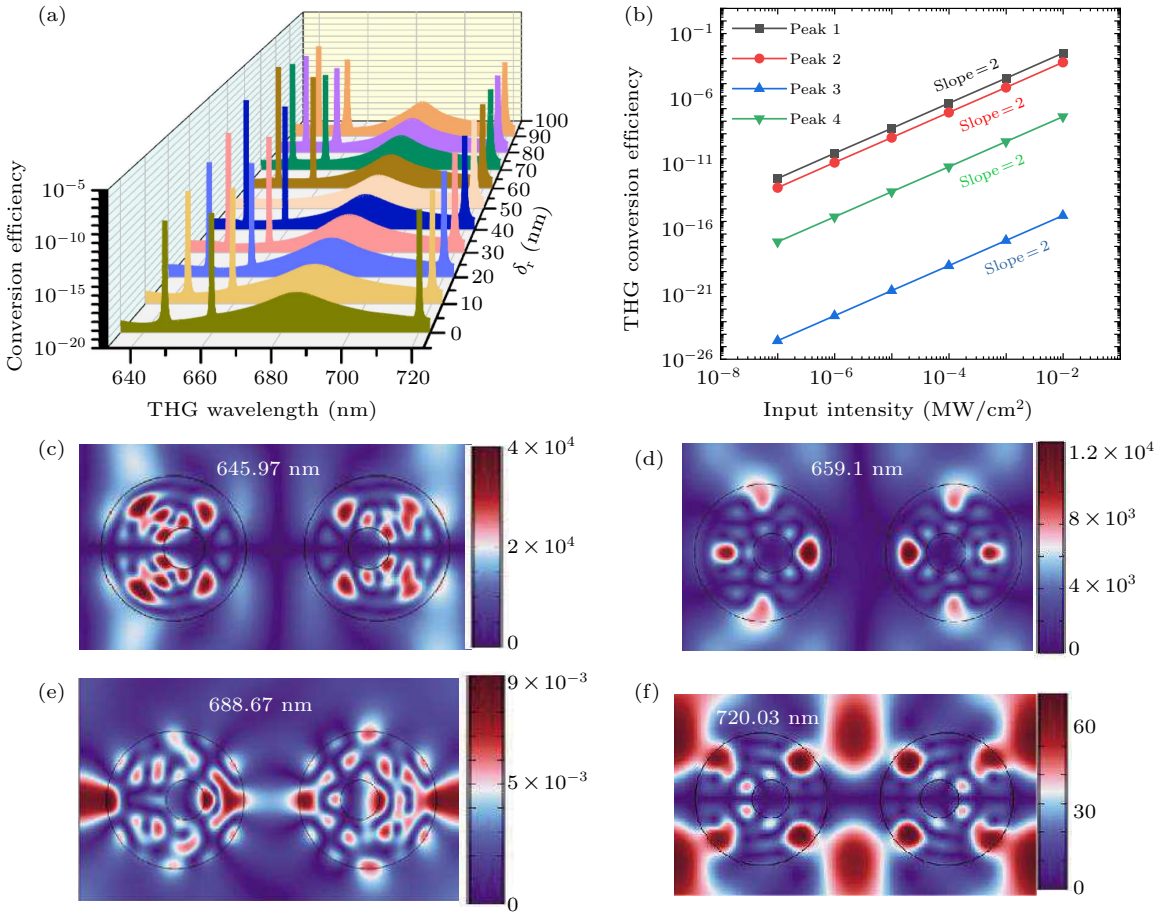


Fig. 9. (a) THG conversion efficiency dependence on THG wavelength and offset δ_r. (b) THG conversion efficiency in relation to the intensity of the base light input at $\delta_r = 40$ nm. All slopes are 2. Meanwhile, (c)–(f) display the THG electric field distributions of the unit V/m in the resonant states at $\delta_r = 40$ nm, respectively.

air holes are shifted the same amount, the two nanorods have a mirror symmetry about the y-axis. At an eigenfrequency around 154.77 THz (Fig. 7(c)) and 151.53 THz (Fig. 7(d)), there is no net polarization along y-axis and no radiation as BICs, while at the eigenfrequency 138.82 THz (Fig. 7(e)), the net polarization along y-axis is not zero, and thus has the radiation of finite Q-factor, i.e., quasi-BICs. So the BICs are formed at $k_x = 0$ in the first two bands. While when $\delta_l \neq \delta_r$, the two symmetry-protected BICs transform into quasi-BICs due to the symmetry breaking, and three quasi-BICs of finite Q-factor appear (Fig. 7(g)). We fix the $\delta_l = 50$ nm to the right direction and the δ_r of values 0 to 90 nm to the left direction. The linear optical transmission in such a structure is illustrated in Fig. 8(a). The transmission spectra around the four modes in the nanostructures of different δ_r are shown in Figs. 8(b)–8(e). When $\delta_l = \delta_r = 50$ nm, only quasi-BIC III is observed, while when $\delta_l \neq \delta_r$, the three quasi-BICs appear and the lineshape becomes broader as δ_r is far away from 50 nm. The dependence of Q-factors of the four modes on the δ_r is shown in Fig. 8(f). The results obey the conclusions arrived from the eigenfrequency analysis.

The THG response in such configurations is shown in Fig. 9(a). The highest THG conversion efficiency occurs at the quasi-BIC I mode when the δ_r is close to 50 nm. It reaches a value of 5.5×10^{-3} in the nanostructure of $\delta_r = 60$ nm. The dependence of THG conversion efficiency on the fundamental intensity in the nanostructure of $\delta_r = 40$ nm at the four resonant modes is given in Fig. 9(b). The corresponding distributions of THG electric field are shown in Figs. 9(c)–9(f), respectively.

We present the reported data about the third harmonic conversion efficiency of other Si structures in Table 1. The results show that the third harmonic conversion efficiency of our designed hollow silicon nanostructures is significantly higher than that of other Si nanostructures.

Table 1. Third harmonic conversion efficiency of other nanostructures prepared in Si.

Structure	TH wavelength (nm)	Pump intensity	Conversion efficiency	Ref.
Silicon nanophotonic waveguide	509	65.93 GM/cm^2	1.93×10^{-6}	[46]
Silicon nanophotonic waveguides	514	39.04 GM/cm^2	1.36×10^{-6}	[46]
Silicon dimer-hole membrane metasurfaces	503.3	$\sim$ 1 GM/cm^2	3.6×10^{-6}	[47]
Thin Si metasurfaces	309	13.3 GM/cm^2	6.12×10^{-5}	[48]
Metal–silicon hybrid metasurface	467.3	$\sim$ 42.5 MW/cm^2	5.2×10^{-11}	[49]
Crystalline silicon metasurface	280	15 GW/cm^2	5.2×10^{-6}	[50]
C-shaped Si nanoantenna-based metasurface	467	$\sim$ 33 GW/cm^2	1.1×10^{-4}	[51]
2D silicon photonic crystal slabs (PCSs)	661	5.3 GW/cm^2	2.1×10^{-6}	[52]
Nano-cuboid metasurface of the amorphous silicon	343	0.7 GW/cm^2	1.13×10^{-5}	[53]
Si metasurface on a gold mirror	417	0.4 GW/cm^2	1.8×10^{-6}	[54]
Si nanorod arrays with hole	719.8	2.65 kW/cm^2	9.6×10^{-2}	this work

4. Conclusion

We numerically demonstrate the quasi symmetry-protected and Brillouin zone folding driven BICs, along with the efficient THG in the symmetry-broken hollow Si nanorod arrays. Two kinds of quasi-BICs are observed when the air holes are shifted away from the center of nanorods in different directions and distances. The THG conversion efficiency reaches a maximum of 10^{-2}, representing an increase of approximately 14 orders of magnitude compared to that in the structure with air pillars positioned at the center of the Si pillars. The results are crucial for comprehending nonlinear optical phenomena and designing nonlinear photonic devices.

Acknowledgment

Project supported by the National Natural Science Foundation of China (Grant Nos. 12174228 and 12274271).

References

[1] Boyd R W 2003 *Nonlinear Optics* (2nd Edn.) (San Diego: Academic Press) pp. 1–577
[2] Zou H W, Zhang C, Du Z H, Wang X Y, Wang H P, Song G B, Zhang Y F, Zhang H, Gao Y H, Wu B, Gao S M and Xu J 2023 *Opt. Express* **31** 34034
[3] Li G X, Li T, Liu H, Li K F, Wang S M, Zhu S N and Cheah K W 2011 *Appl. Phys. Lett.* **98** 261909
[4] Warren-Smith S C, Chemnitz M, Schneidewind H, Kostecki R, Ebendorff-Heidepriem H, Monro T M and Schmidt M A 2017 *Opt. Lett.* **42** 1812
[5] Miyazaki S, Leproux P, Couderc V, Hayashi Y and Kano H 2020 *Appl. Phys. Express* **13** 072002
[6] Farrar M J, Wise F W, Fetcho J R and Schaffer C B 2011 *Biophys. J.* **100** 1362
[7] Tokarz D, Cisek R, Wein M N, Turcotte R, Haase C, Yeh S C A, Bharadwaj S, Raphaelet A P, Paudel H, Alt C, Liu T M, Kronenberg H M and Lin C P 2017 *PLoS One* **12** e0186846
[8] Zalogina A, Carletti L, Rudenko A, Moloney J V, Tripathi A, Lee H C, Shadrivovet I, Park H G, Kivshar Y and Kruk S 2023 *Sci. Adv.* **9** eadg2655
[9] Liu T T, Qin M B, Wu F and Xiao S Y 2023 *Phys. Rev. B* **107** 075441
[10] Frigenti G, Farnesi D, Nunzi Conti G and Soria S 2020 *Micromachines* **11** 303
[11] Wu F, Liu T T, Yang L, Xiao S Y and Chen G Y 2023 *Phys. Rev. B* **107** 165428
[12] Wu F, Qi X, Luo M, Liu T T and Xiao S Y 2023 *Phys. Rev. B* **108** 165404
[13] Ning T Y, Li X, Zhao Y, Yin L Y, Huo Y Y, Zhao L N and Yue Q Y 2020 *Opt. Express* **28** 34024
[14] Fedotov V A, Rose M, Prosvirnin S L, Papasimakis N and Zheludev N I 2007 *Phys. Rev. Lett.* **99** 147401

[15] Campione S, Liu S, Basilio L I, Warne L K, Langston W L, Luk T S, Wendt J R, Reno J L, Keeler G A, Brener I and Sinclair M B 2016 *ACS Photonics* **3** 2362

[16] Li J T, Li J, Zheng C L, Yue Z, Wang S L, Li M Y, Zhao H L, Zhang Y T and Yao J Q 2021 *Carbon* **182** 506

[17] Carletti L, Koshelev K, De Angelis C and Kivshar Y 2018 *Phys. Rev. Lett.* **121** 033903

[18] Ning T Y, Li X, Zhang Z S, Huo Y Y, Yue Q Y, Zhao L N and Gao Y M 2021 *Opt. Express* **29** 17286

[19] Wang B K, Liu J, Cui J H, Liu J L, Tian F J, Sun W M and Li L 2023 *Front. Phys.* **11** 1135211

[20] Wu F, Wu J J, Guo Z W, Jiang H T, Sun Y, Li Y H, Ren J and Chen H 2019 *Phys. Rev. Appl.* **12** 014028

[21] Tang H Z, Hu P, Cui D J, Xiang H and Han D Z 2022 *Chin. Phys. B* **31** 104209

[22] Yang J L, Shi A Q, Peng Y C, Peng P and Liu J J 2024 *Chin. Phys. B* **33** 084206

[23] Xiao X, Li Z Y, Chu T, Xu H, Li X Y, Nemkova A, Kang X, Yu Y D and Yu J Z 2013 *Sci. China Technol. Sci.* **56** 586

[24] Witzens J 2018 *Proc. IEEE* **106** 2158

[25] Ikeda K, Suzuki K, Konoike R, Namiki S and Kawashima H 2020 *Opt. Commun.* **466** 125677

[26] Izhaky N, Morse M T, Koehl S, Cohen O, Rubin D, Barkai A, Sarid G, Cohen R and Paniccia M J 2006 *IEEE J. Sel. Top. Quantum Electron.* **12** 1688

[27] Galland C, Novack A, Liu Y, Ding R, Gould M, Baehr-Jones T, Li Q, Yang Y S, Ma Y J, Zhang Y, Padmaraju K, Bergmen K, Lim A E J, Lo G Q and Hochberg M 2013 *Proc. SPIE* **8767** 87670G

[28] Szelag B, Hassan K, Adelmini L, Ghegin E, Rodriguez P, Nemouchi F, Brianceau P, Vermande E, Schembri A, Carrara D, Cavalié P, Franchin F, Roure M C, Sanchez L, Jany C and Olivier S 2019 *IEEE J. Sel. Top. Quantum Electron.* **25** 1

[29] González-Fernández A A, Aceves-Mijares M, Pérez-Díaz O, Hernández-Betanzos J and Domínguez C 2021 *Crystals* **11** 630

[30] Moss D J, Morandotti R, Gaeta A L and Lipson M 2013 *Nat. Photonics* **7** 597

[31] Pavesi L, Gaburro Z, Dal Negro L, Bettotti P, Prakash G V, Cazzanelli M and Oton C J 2003 *Opt. Lasers Eng.* **39** 345

[32] Wiecha P R, Arbouet A, Kallel H, Periwal P, Baron T and Paillard V 2015 *Phys. Rev. B* **91** 121416

[33] Leuthold J, Koos C and Freude W 2010 *Nat. Photonics* **4** 535

[34] Yang J L, Yuan Q C, Chen R F, Fang H L, Xiao F J, Li J T, Jiang B Q, Zhao J L and Gan X T 2019 *Acta Phys. Sin.* **68** 214207 (in Chinese)

[35] Sun L, Zhang Y, He Y, Wang H W and Su Y K 2020 *Nanophotonics* **9** 1321

[36] Dharanipathy U P, Minkov M, Tonin M, Savona V and Houdré R 2014 *Appl. Phys. Lett.* **105** 101101

[37] Choi W K, Liew T H, Dawood M K, Smith H I, Thompson C V and Hong M H 2008 *Nano Lett.* **8** 3799

[38] Xie M, Wang J S, Fan Z Y, Lu J G and Yap Y K 2008 *Nanotechnology* **19** 365609

[39] Chen L, Liu Z T, Gu C, Xu X and Yang Y 2006 *Adv. Mater.* **18** 228

[40] Li H L, Ye T C, Shi L N and Xie C Q 2017 *Journal of Micromechanics and Microengineering* **27** 124002

[41] Marty F, Rousseau L, Saadany B, Mercier B, Français O, Mita Y and Bourouina T 2005 *Microelectronics Journal* **36** 67

[42] Chang S W, Chuang V P, Boles S T, Ross C A and Thompson C V 2009 *Adv. Funct. Mater.* **19** 249

[43] Li H H 1980 *J. Phys. Chem. Ref. Data* **9** 561

[44] Aspnes D E and Studna A A 1983 *Phys. Rev. B* **27** 985

[45] Ning T Y, Zhao L N, Huo Y Y, Cai Y J and Ren Y Y 2023 *Nanophotonics* **12** 4009

[46] Sederberg S, Firby C J and Elezzabi A Y 2019 *Opt. Express* **27** 4990

[47] Zheng Z, Xu L, Huang L J, Smirnova D, Kamali K Z, Yousefi A, Deng F, Camacho-Morales R, Ying C, Miroshnichenko A E, Neshev D N and Rahmani M 2023 *Opto-Electron. Adv.* **6** 220174

[48] Deng Y H, Shi Z H, Zheng Y Q, Zhang H J, Li H Y, Li S Y and Zhou Z K 2024 *Adv. Sci.* **11** 2404094

[49] Li Y, Zhang G Q, Tang Y T, Zhang X C, Cai W F, Liu Y J, Cao T and Li G X 2022 *Nanophotonics* **11** 2245

[50] Abdelraouf O A M, Anthur A P, Wang X R, Wang Q J and Liu H 2024 *ACS Nano* **18** 4388

[51] Gao Y S, Fan Y B, Wang Y J, Yang W H, Song Q H and Xiao S M 2018 *Nano Lett.* **18** 8054

[52] Ban G X, Gong C, Zhou C B, Li S Y, Barille R, Liu X J and Wang Y 2019 *Opt. Lett.* **44** 126

[53] Tang W J, Zhao Q M, Wang Z Y, Gao Y J, He J, Zhu Y, Wang S X, Yu H H, Peng R W and Wang M 2024 *Opt. Lett.* **49** 1169

[54] Yang G C, Dev S U, Allen M S, Allen J W and Harutyunyan H 2022 *Nano Lett.* **22** 2001